IOP Publishing Phys. Med. Biol. 69 (2024) 055003 https://doi.org/10.1088/1361-6560/ad247d

Physics in Medicine & Biology

IPEM Institute of Physics and Engineering in Medicine

OPEN ACCESS

RECEIVED
10 August 2023

REVISED
12 January 2024

ACCEPTED FOR PUBLICATION
31 January 2024

PUBLISHED
19 February 2024

PAPER

Mini-GRID radiotherapy on the CLEAR very-high-energy electron beamline: collimator optimization, film dosimetry, and Monte Carlo simulations

Nathan Clements[1], **Nolan Esplen**[1], **Joseph Bateman**[2], **Cameron Robertson**[2], **Manjit Dosanjh**[2,3], **Pierre Korysko**[2,3], **Wilfrid Farabolini**[3], **Roberto Corsini**[3] and **Magdalena Bazalova-Carter**[1]

[1] Department of Physics and Astronomy, University of Victoria, Victoria, BC, Canada
[2] Department of Physics, University of Oxford, Oxford, United Kingdom
[3] CERN, Geneva, Switzerland

E-mail: nclements@uvic.ca

Keywords: GRID, FLASH, very-high-energy electrons, Monte Carlo simulation, film dosimetry, spatially-fractionated radiotherapy

Abstract

Objective. Spatially-fractionated radiotherapy (SFRT) delivered with a very-high-energy electron (VHEE) beam and a mini-GRID collimator was investigated to achieve synergistic normal tissue-sparing through spatial fractionation and the FLASH effect. *Approach.* A tungsten mini-GRID collimator for delivering VHEE SFRT was optimized using Monte Carlo (MC) simulations. Peak-to-valley dose ratios (PVDRs), depths of convergence (DoCs, PVDR $\leqslant$ 1.1), and peak and valley doses in a water phantom from a simulated 150 MeV VHEE source were evaluated. Collimator thickness, hole width, and septal width were varied to determine an optimal value for each parameter that maximized PVDR and DoC. The optimized collimator (20 mm thick rectangular prism with a 15 mm $\times$ 15 mm face with a 7 $\times$ 7 array of 0.5 mm holes separated by 1.1 mm septa) was 3D-printed and used for VHEE irradiations with the CERN linear electron accelerator for research beam. Open beam and mini-GRID irradiations were performed at 140, 175, and 200 MeV and dose was recorded with radiochromic films in a water tank. PVDR, central-axis (CAX) and valley dose rates and DoCs were evaluated.
Main results. Films demonstrated peak and valley dose rates on the order of 100 s of MGy/s, which could promote FLASH-sparing effects. Across the three energies, PVDRs of 2–4 at 13 mm depth and DoCs between 39 and 47 mm were achieved. Open beam and mini-GRID MC simulations were run to replicate the film results at 200 MeV. For the mini-GRID irradiations, the film CAX dose was on average 15% higher, the film valley dose was 28% higher, and the film PVDR was 15% lower than calculated by MC. *Significance.* Ultimately, the PVDRs and DoCs were determined to be too low for a significant potential for SFRT tissue-sparing effects to be present, particularly at depth. Further beam delivery optimization and investigations of new means of spatial fractionation are warranted.

1. Introduction

Radiation therapy (RT) is prescribed to cancer patients with the intent to cure or for palliation. In either case, the objective of treatment is to maximize damage to cancer cells while minimizing side effects for the patient in particular, due to damage in critical organs. Spatially-fractionated radiotherapy (SFRT) and FLASH RT delivered at ultra-high dose rates (UHDRs) are two new non-standard radiotherapy techniques of great interest in modern oncology due to the distinct normal-tissue-sparing effects they can each elicit. Recent discussion has arisen on a possible synergy between the two techniques which could potentially result in the increase of their individual therapeutic windows (Schneider *et al* 2022). However, research on potential delivery methods to achieve the two tissue-sparing effects in deep-seated tumours simultaneously is needed. This study investigates

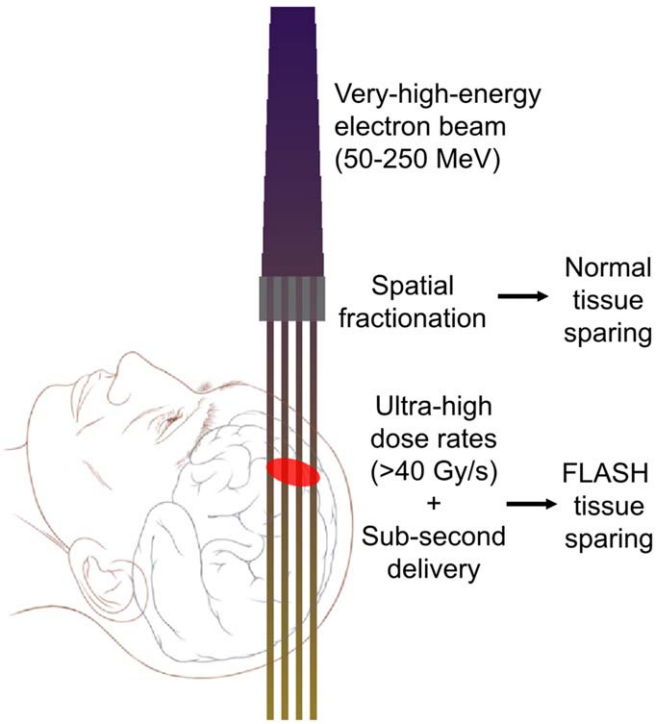

Figure 1. A conceptual diagram for combining FLASH RT and spatially-fractionated RT using a very-high-energy electron source.

the feasibility of UHDR mini-GRID (GRID with mini beams) radiotherapy using a very-high-energy electron (VHEE) source.

SFRT is a technique which employs non-uniform dose distributions, in particular, alternating low- and high-dose regions, typically achieved via collimation. The 2D collimated form of SFRT is known as GRID therapy due to the grid pattern it produces. Today, SFRT and GRID therapy are used to treat patients with limited local control options, including patients with advanced cancers, bulky tumours, and or radioresistant tumours (Neuner *et al* 2012, Billena and Khan 2019, Choi *et al* 2019, Yan *et al* 2020, Owen *et al* 2022). Relative to standard RT, SFRT techniques offer a high biologically effective dose (BED) and the capacity to reduce normal tissue toxicity (Mohiuddin *et al* 1999, Yan *et al* 2020) without reducing the effectiveness of tumour treatment. The preferential normal-tissue sparing is hypothesized to be a result of bystander effects (Widel 2016), differential vascular damage, and anti-tumour immune responses (Yan *et al* 2020). Although the radiobiological mechanisms behind the reduction in toxicity are not entirely known, minimizing valley dose and maximizing peak-to-valley dose ratio (PVDR) has been shown to be linked to the normal tissue sparing potential (Dilmanian *et al* 2002, Smyth *et al* 2016). However, particle type and beamlet size have been shown to affect which dosimetric quantities do in fact indicate normal tissue sparing (Fernandez-Palomo *et al* 2022).

While SFRT presents a change to the spatial structure of radiotherapy treatment, FLASH RT presents a change to the temporal structure of treatment delivery. FLASH RT is characterized by the effect that it produces, lesser toxicity to normal tissue without compromising tumour control. Though the biological mechanisms behind the effect are not entirely understood, FLASH RT is primarily a combination of UHDRs and rapid treatment times ($<$0.1 s) (Esplen *et al* 2020, Wilson *et al* 2020). Numerous animal (mice, mini pigs, and cats) and tissue (brain, neural stem cells, and skin) studies have shown that sub-second, UHDR treatment can reduce toxicity to healthy tissue without compromising tumour treatment (Levy *et al* 2019, Vozenin *et al* 2019, 2019). Presently, radiolytic oxygen depletion and transient cellular hypoxia, perhaps constrained to hypoxic (i.e. stem) cell compartments, and radical recombination are favoured radiobiological hypotheses for the effect (Adrian *et al* 2020, Labarbe *et al* 2020, Bronk *et al* 2022), but may not entirely account for the observed effects *in vivo* (Zhou *et al* 2020, Boscolo *et al* 2021). The dosimetric and temporal conditions needed for the FLASH effect remain to be fully understood and while the average dose rate and the timescale of irradiation appear to also be important, the exact parameters remain uncertain and appear to be multifactorial (Ruan *et al* 2021, Böhlen *et al* 2022). A conceptual diagram showing UHDR SFRT using a VHEE source is presented in figure 1.

Sub-second FLASH irradiations synergize well with spatially-fractionated techniques, given that loss of spatial fractionation often occurs as a result of organ motion due to treatment times longer than physiological motion. The normal tissue-sparing effects of FLASH RT and SFRT are thought to occur through different

biological mechanisms (Schneider *et al* 2022) and thus have different physical and delivery requirements; as an example, SFRT does not seem to have the same requirements on the beam time structure, threshold dose, irradiation time, and tissue oxygen concentration that FLASH radiotherapy does (Dilmanian *et al* 2003, Adrian *et al* 2020, Vozenin *et al* 2020, Wilson *et al* 2020). Therefore, future studies using sources that are capable of spatially-fractionated and open beam UHDR irradiations could help determine the potential for combining the techniques and determining to what degree each technique contributes should the effects synergize (Wright *et al* 2021). Only a few low-energy x-rays with steep dose fall-off with depth generated by synchrotrons have shown the capacity for UHDR micro-fractionation delivery (Smyth *et al* 2018, Montay-Gruel *et al* 2022). Other sources with the potential for combining FLASH and SFRT need to be investigated, especially since the list of particle types and beam energies that are UHDR-compatible continues to grow (4.5 and 224 MeV protons (Beyreuther *et al* 2019, Buonanno *et al* 2019), MeV photons (Esplen *et al* 2022), keV photons (Bazalova-Carter and Esplen 2019), MeV electrons (Favaudon *et al* 2014, Vozenin *et al* 2019), very-high-energy electrons (Rahman *et al* 2022), He ions (Tessonnier *et al* 2021)).

In this study, very-high-energy electron beams (VHEE, 50–250 MeV) are considered for radiotherapy (DesRosiers *et al* 2000, Papiez *et al* 2002, Yeboah *et al* 2002, Yeboah and Sandison 2002, DesRosiers *et al* 2008). VHEE beams are a newer particle source in radiation oncology studies, their low sensitivity to tissue inhomogeneities compared to photon and proton beams and their high penetration depth as compared to clinical 4–20 MeV electron beams make them appealing sources from a physics perspective (Bazalova-Carter *et al* 2015, Palma *et al* 2016, Schüler *et al* 2017, Whitmore *et al* 2021). In terms of FLASH-compatibility, VHEE sources readily achieve UHDRs, even at modest beam currents, and can easily perform sub-second irradiations (Schüler *et al* 2022). For performing SFRT, VHEE sources are advantageous due to their low lateral scatter, as compared to lower energy electron sources (Martínez-Rovira *et al* 2015, Clements *et al* 2023). One potential complication with VHEEs and a tungsten collimator is that the radiation yield of 200 MeV electrons in tungsten is ∼84% (Berger *et al* 1999) and therefore it is expected that the collimator will also serve as a source of Bremsstrahlung x-rays. A similar work presented by Pensavalle]*et al* showed that the Bremsstrahlung dose was 10% of the electron dose in the peak regions for a 9 MeV beam impinging on a 5 mm tungsten target. The 9 MeV radiation yield is 28% and therefore the Bremsstrahlung contribution in our work is expected to be higher. However, since our proposed tungsten collimator is 2 cm thick, it will completely attenuate some of the generated Bremsstrahlung x-rays. In addition, the high mass collisional stopping power of 200 MeV electrons and the low mass energy absorption coefficient of Bremsstrahlung x-rays in water will cause a 200 MeV electron to deposit more dose compared to a Bremsstrahlung x-ray (Dunning and Bazalova-Carter 2019) and the effect of Bremsstrahlung dose will be mitigated to a degree. Due to these competing effects, predicting the significance of the Bremsstrahlung dose is not a simple task.

This work investigates the feasibility of UHDR mini-GRID radiotherapy using a VHEE source, a technique which could further widen the therapeutic windows of radiation therapy if capable of synergizing FLASH RT and SFRT. First, a mini-GRID collimator is optimized and 3D-printed for mini-GRID film dosimetry with a UHDR VHEE source. For the purpose of this work, Monte Carlo (MC) simulations are employed for an accurate representation of the irradiation setup. Finally, MC simulations of the experimental mini-GRID irradiation setup are presented. Due to the limitations in the current size of VHEE sources, in this study, we focus on small VHEE SFRT fields.

2. Materials and methods

2.1. CLEAR VHEE beamline

The CERN linear electron accelerator for research (CLEAR) beamline comprises a VHEE linear accelerator capable of producing electron beams with energies between 60 and 220 MeV and provides tunability for a large number of beam parameters, as indicated in table 1 (Korysko *et al* 2023)).

The beamline can readily achieve UHDR conditions compatible with FLASH studies (Corsini *et al* 2021). The user facility for experimentation consists of an In-Air Test Area. The CLEAR-Robot (C-Robot) can be installed in this area, which includes three independent linear motion stages (in x, y, and z), a grabber, and a camera which assists in the moving of samples in and out of a polymethyl methacrylate (PMMA) water tank centred in the beam path (Korysko *et al* 2023). The water tank is capable of holding 3D-printed radiochromic film holders of various lengths in which films (35 mm × 40 mm) can be spaced at 0.5 cm intervals (Korysko *et al* 2023). First, a simplified particle representing the CLEAR VHEE electron beam was used as the particle source for the mini-GRID collimator optimization. Next, open beam and mini-GRID irradiations were performed using the mini-GRID collimator on the CLEAR beamline and modelled by MC.

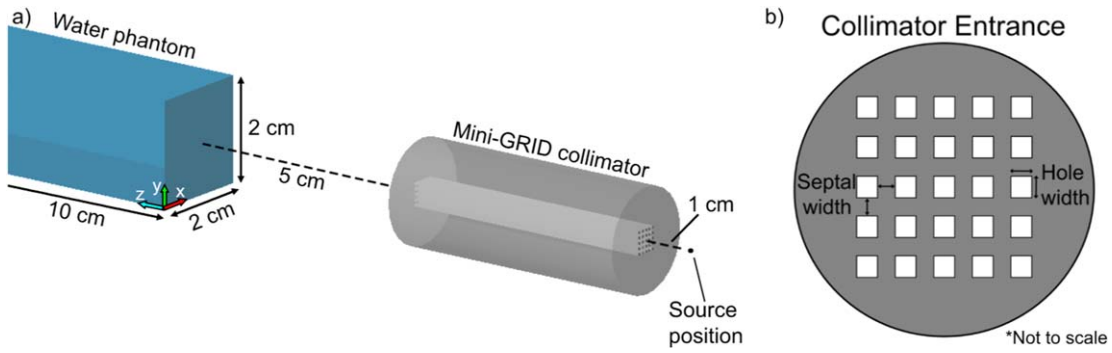

Figure 2. (a) Labelled diagram of Monte Carlo simulation geometry for collimator optimization. (b) 2D view of mini-GRID collimator entrance face with hole width and septal width indicated.

Table 1. CLEAR beam parameters.
Adapted from Korysko *et al* 2023. CC BY 4.0.

Parameters	Values
Beam energy	30–220 MeV
Beam energy spread	<0.2% rms
Bunch length rms	0.1–10 ps
Bunch frequency	1.5 or 3.0 GHz
Bunch charge	0.005–1.6 nC
Norm. emittance	1–20 μm
Bunches per pulse	1–200
Max. pulse charge	87 nC
Repetition rate	0.8333–10 Hz

2.2. Mini-GRID collimator optimization

An optimized mini-GRID collimator would ideally maximize PVDR and minimize valley dose since these have all been shown to be driving factors in maximizing the tissue-sparing effects seen in SFRT (Dilmanian *et al* 2002, Fernandez-Palomo *et al* 2022).

The CERN mini-GRID collimator was designed and optimized using TOPAS (v3.6) MC simulations (Perl *et al* 2012, Faddegon *et al* 2020) and the process outlined below was similar to previous work (Clements *et al* 2022). To achieve 2D minibeam spatial fractionation, a mini-GRID collimator made of tungsten was simulated for use on the CLEAR beamline.

Dose was scored in a rectangular (2 cm $\times$ 2 cm $\times$ 10 cm) water phantom. A simplified VHEE source, based on the capabilities of CLEAR, was modelled as a non-divergent 150 MeV Gaussian electron beam with $\sigma_x = \sigma_y = 2.55$ mm located 1 cm upstream from the mini-GRID collimator (Poppinga *et al* 2020). The mini-GRID collimator was initially defined as a cylindrical body of tungsten with a 1cm radius and an array of 25 parallel square holes arranged in a 5 $\times$ 5 square pattern. Three geometric parameters of the mini-GRID collimator were optimized: (1) the thickness (the dimension along the beam axis), (2) the hole width, and (3) the septal width (thickness of tungsten between holes) (see figure 2(b)). The optimization was performed by exploring a range of values for each parameter while the others were held constant. The values tested for each parameter are presented in table 2 along with the 'default' collimator parameter values designated with an asterisk. Each parameter space was tested with the other two collimator parameters set to their 'default' value. For all simulations, the World was composed of air, the source-to-collimator distance (SCD) was held at 1 cm, and the collimator-to-surface distance (CSD) was held at 5 cm. The geometric setup for the simulations is shown in figure 2(a).

The mean dose to medium per electron was scored in a water phantom in (0.1 mm $\times$ 0.1 mm $\times$ 5 mm) voxels with the larger voxel dimension along the beam direction (depth into the water phantom) for 1×10^6 electron histories. The mean dose per electron was then divided by the fundamental charge in nC to obtain the dose per nC. Standard deviation was also scored, and MC uncertainty for the calculated quantities was determined to be <1%.

The grid-averaged peak dose per charge, valley dose per charge, and PVDR were calculated as functions of depth in the water phantom. The 25 peaks of the phantom surface layer were found using local maxima finding with threshold dose per charge values and spacing between peaks as additional constraints. Valleys were

Table 2. GRID collimator parameters to be optimized with bold values indicating 'default' parameters.

Optimization parameters	Values (mm)
Thickness	30, **50**, 70, 90, 110
Hole width	0.3, **0.5**, 0.7, 0.9, 1.1
Septal width	0.3, **0.5**, 0.7, 0.9, 1.1

similarly identified. The mean peak dose per charge was calculated as the mean of 250.3 mm × 0.3 mm areas and the mean valley dose per charge was calculated as the mean of 80.1 mm × x mm areas where x was the field size of the grid-patterned dose distribution. The uncertainty was taken as the standard error of the ROIs for the mean peak dose per charge and mean valley dose per charge. The peak and valley finding algorithm was used for the first depth alone and then propagated throughout the phantom since the source and collimator holes were parallel.

The PVDR was calculated as

$$\mathrm{PVDR} = \frac{\left\langle \left(\frac{D}{q}\right)_{\mathrm{peak}} \right\rangle}{\left\langle \left(\frac{D}{q}\right)_{\mathrm{valley}} \right\rangle} \tag{1}$$

where $\langle \left(\frac{D}{q}\right)_{\mathrm{peak}} \rangle$ is the mean peak dose per charge and $\langle \left(\frac{D}{q}\right)_{\mathrm{valley}} \rangle$ is the mean valley dose per charge, both calculated as detailed above. The error on the PVDR was calculated as follows:

$$\Delta\mathrm{PVDR} = \mathrm{PVDR} \times \sqrt{\left(\frac{\Delta\left\langle \left(\frac{D}{q}\right)_{\mathrm{peak}} \right\rangle}{\left\langle \left(\frac{D}{q}\right)_{\mathrm{peak}} \right\rangle}\right)^2 + \left(\frac{\Delta\left\langle \left(\frac{D}{q}\right)_{\mathrm{valley}} \right\rangle}{\left\langle \left(\frac{D}{q}\right)_{\mathrm{valley}} \right\rangle}\right)^2} \tag{2}$$

where $\Delta\langle \left(\frac{D}{q}\right)_{\mathrm{peak}} \rangle$ and $\langle \left(\frac{D}{q}\right)_{\mathrm{peak}} \rangle$ are the standard error and the mean of the peak dose per charge, $\Delta\langle \left(\frac{D}{q}\right)_{\mathrm{valley}} \rangle$ and $\langle \left(\frac{D}{q}\right)_{\mathrm{valley}} \rangle$ are the standard error and mean of the valley dose per charge.

Based on the results of the mini-GRID collimator optimization (see section 3.1), the tungsten collimator was 3D printed (M&I Materials, Manchester, UK) as a 20 mm thick rectangular prism with a 15 mm × 15 mm face with a 7 × 7 array of 0.5 mm holes separated by 1.1 mm septa (see figure 3(a)). Note that this was a larger set of holes compared to the MC-simulated collimator. The array was enlarged to cover a larger field size to alleviate potential experimental alignment issues.

The TOPAS physics module used in the collimator optimization was the 'g4em-standard-opt4' package and the particle cutoff distance was set to 0.1 mm for all particles, all other physics parameters were left as their default (Perl *et al* 2012, Faddegon *et al* 2020).

2.3. Film dosimetry setup at CLEAR

The experimental setup for film irradiations consisted of a vacuum beamline, a 200 μm thick yttrium aluminum garnet (YAG) scintillation screen that was used as a scatterer for beam enlargement, a 0.1 mm Kapton exit window, the mini-GRID collimator (see section 2.2), and a water tank in which film holders could be precisely placed using the multi-axis CLEAR robot (Korysko *et al* 2023). Films (35 mm × 40 mm) were placed in multi-film stack phantoms, which were inserted into the tank and then irradiated by the beam (figure 3(c)).

The mini-GRID collimator was placed on a motion stage and was centred on the incoming beam using a laser. The mini-GRID collimator and the film holders were placed as close to the entrance of the water phantom as possible to maximize PVDR. The films used were GAFchromic EBT3 films (Ashland Inc., Wayne, NJ, USA), which have a dynamic dose range between 0.1 and 20 Gy (GAFChromic EBT3 Film Specifications,). These films were selected for UHDR VHEE dosimetry due to their dose-rate independence, high spatial and dose accuracy ($\leqslant$1% error) and the suitability of their dose range for capturing the low valley doses while aiming for ~15 Gy in the central beamlet of the GRID dose distribution (Bazalova-Carter *et al* 2015, Casolaro *et al* 2019). Films were placed in holders with spacings between films of either 0.5 or 1 cm.

UHDR irradiations were performed with and without the mini-GRID collimator in place for energies of 140, 175, and 200 MeV. For the open beam (without the mini-GRID collimator) irradiations, the total charge

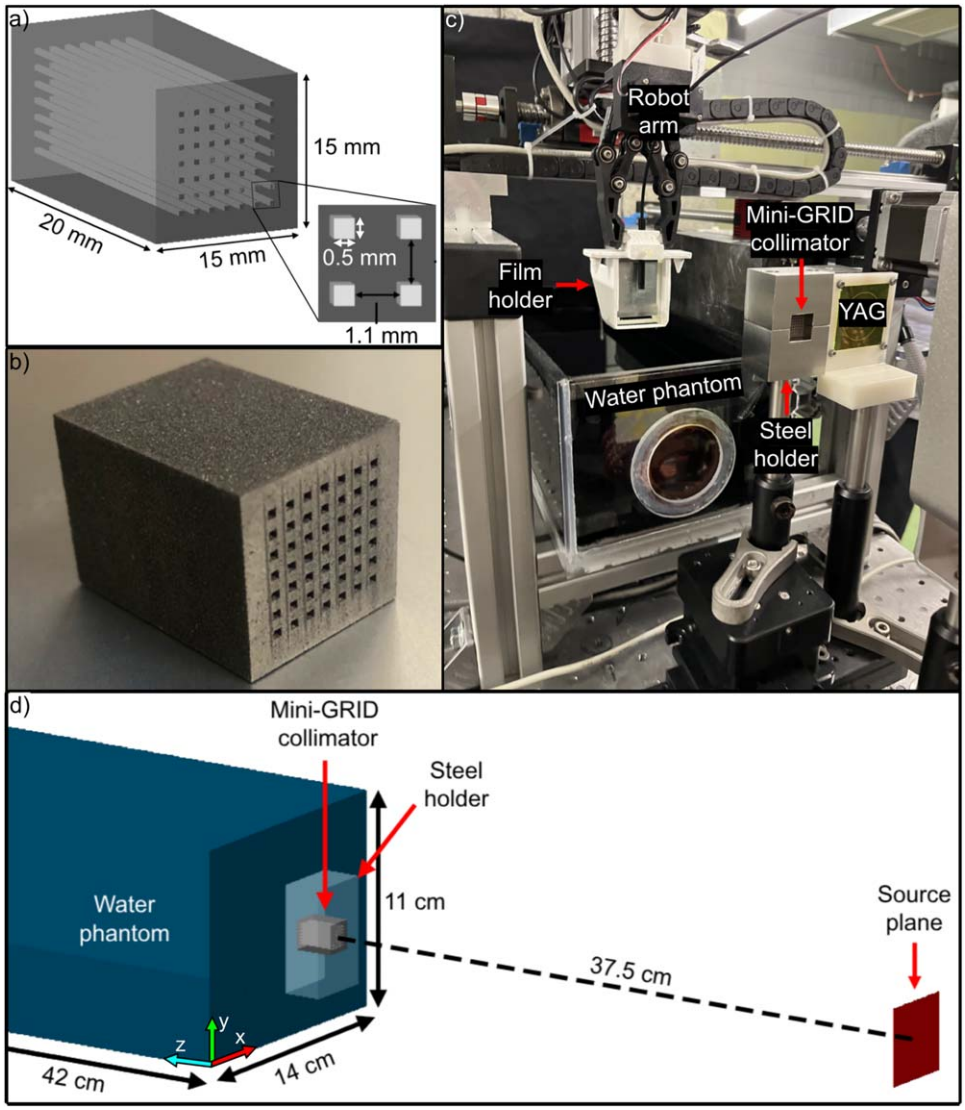

Figure 3. (a) Diagram of the mini-GRID collimator design. (b) Photo of the 3D printed tungsten mini-GRID collimator. (c) Photo of the film irradiation setup at CLEAR. (d) The simulation setup for CLEAR irradiations.

required to deliver a maximum of ~15 Gy was determined by the beam operators (based on previous operational and experimental experience[4]). For the mini-GRID irradiations, the open beam charges were scaled down by a factor given by the central peak dose ratio between MC simulations with and without the mini-GRID collimator. The beam energy, beam size, charge delivered, bunch charge, bunch frequency, and repetition rate for each irradiation are presented in table 3.

In addition to the films in the water tank, at least one background film was left in a holder beside the water tank for each irradiation to measure any dose that may have been delivered to the films as the beam was being adjusted to the desired parameters or from beam losses during sub-optimal low-energy acceleration runs.

2.4. Film analysis

After irradiation, the films were placed in a light-tight envelope overnight and scanned after 24 hrs using a Perfection V800 flatbed scanner (Epson, Suwa, Japan) at 300 dpi resolution. The green channel scanned films were then analyzed using a custom Python script. The equation used to convert from the green colour intensity to dose was:

$$D = \frac{(a - cX)}{(X - b)}, \tag{3}$$

[4] Personal communication with Pierre Korysko and Wilfrid Farabolini.

Table 3. Beam parameters for three sets of mini-GRID and open beam (OB) film irradiations at CLEAR.

Beam parameters	#1	#2	#3
Energy (MeV)	199.4 (~200)	175	140
Size σ_x, σ_y[a] (mm)	(4.12 ± 0.20, 4.01 ± 0.20)	(4.63 ± 0.26, 4.67 ± 0.27)	(5.70 ± 0.26, 5.50 ± 0.27)
Charge delivered (nC)	Mini-GRID: 8.2, OB: 6.8	Mini-GRID: 7.1, OB: 5.2	Mini-GRID: 19.2, OB: 10.5
Bunch charge (pC)	200	200	~100
Bunch frequency (GHz)	1.5	1.5	1.5
Pulse repetition rate (Hz)	0.8333	0.8333	0.8333

[a] Beam size as measured at 13 mm depth in water.

where D is dose, X is the green colour intensity, and a, b, and c are calibration parameters. The films were calibrated with 5.5 MeV electrons using the eRT6 Oriatron (1 μs pulse width at 10 Hz with a 0.05 Gy s^{-1} mean dose rate) at the centre hospitalier universitaire vaudois (CHUV). It has been shown that the energy response of GAFChromic films is flat for VHEE (Bazalova-Carter *et al* 2015).

Once the delivered dose had been calculated from the film pixel value, the mean dose of the background film was subtracted. The film doses were subsequently converted to dose rate using:

$$\dot{D} = D \cdot \frac{q_{tot}}{q_b} f_b, \tag{4}$$

where $\dot{D}$ is dose rate, D is dose, q_{tot} is the total charge delivered for an irradiation, q_b is the charge per bunch, and f_b is the bunch frequency. Note that in this study, the dose rate considered is the dose rate within a pulse. In the film irradiation component of this study, we used single-pulse dose delivery since the CLEAR beam can deliver high doses in a single pulse, up to ~160 Gy for the beam sizes considered in this work (Hart *et al* 2024).

To examine the effect of depth in water on the central axis (CAX) dose rate (or central peak dose rate), the central beam pixel was found and a 4.2 mm × 4.2 mm area and a 0.25 mm × 0.25 mm area were averaged to determine the mean CAX dose rate for open beam and GRID, respectively. The standard error of the ROIs was taken as the uncertainty. The central pixel of each peak ROI was found using a slight Gaussian blur and a local maxima finder. For mini-GRID irradiations, the effect of depth in water on the valley dose rate was also studied. The valleys were defined as two 0.25 mm × 1.25 mm regions. One was 0.85 mm above the central beam pixel which is 1.25 mm in x and 0.25 mm in y (along the adjacent horizontal valley), and the other was 0.85 mm to the left of the central beam pixel and 0.25 mm in x and 1.25 mm in y (along the vertical valley).

PVDR and its associated error were calculated as per equations (1) and (2) using dose rate instead of dose-per-charge and with the peaks and valleys defined above.

2.5. Monte Carlo simulation of 200 MeV irradiations

The 200 MeV open beam and mini-GRID irradiations performed at CERN were simulated in TOPAS MC. 200 MeV was the energy that was selected due to the beamline being optimized for this energy and it demonstrated the largest depth of convergence.

The MC model included the GRID collimator, the steel holder for the GRID collimator, and the water phantom (the PMMA was approximated as water). Based on measurements, the post-YAG screen scattered beam was defined at the exit window as a 199.4 MeV Gaussian electron beam with a 1 MeV energy spread. The x and y beam position spread and angular spreads were initially based on YAG screen measurements of the beam in air after being scattered by a first YAG screen. Ultimately, the spreads were adjusted until agreement was seen between open beam simulation σ_x and σ_y values and film values. Ultimately, the σ_x and σ_y values were determined as 1.31 mm and 1.91 mm and the x and y angular spreads were set as 0.5168° and 0.5070°, respectively.

Twenty simulations of 5×10^5 primary electrons were run in parallel for both open beam and mini-GRID setups. The mean dose to medium per particle was scored in the (14 cm × 11 cm × 42 cm) water phantom with (0.01 cm × 0.01 cm × 0.025 cm) voxels. Standard deviation was also scored, and MC uncertainty for the calculated quantities was <3%. The x and y voxel size was chosen as 0.1 mm to approximate film readout and the z dimension (depth) was chosen to approximate the thickness of the films (~0.280 mm). To obtain the mean dose, the mean dose to medium per particle for all voxels was divided by the fundamental charge and multiplied by the total charge delivered for the 200 MeV irradiations (6.8 nC for open beam and 8.2 nC for mini-GRID).

As in the film analysis, 1D profiles and CAX dose were compared to the film results for both mini-GRID and open beam simulations. The ROIs (and their size) were selected to be approximately equivalent to those from film analysis. The CAX ROI for the open beam was 1.6 mm × 1.6 mm, and for mini-GRID, the CAX ROI was 0.3 mm × 0.3 mm, and the valleys were two 0.3 mm × 1.4 mm regions, similar to the film analysis. For the open

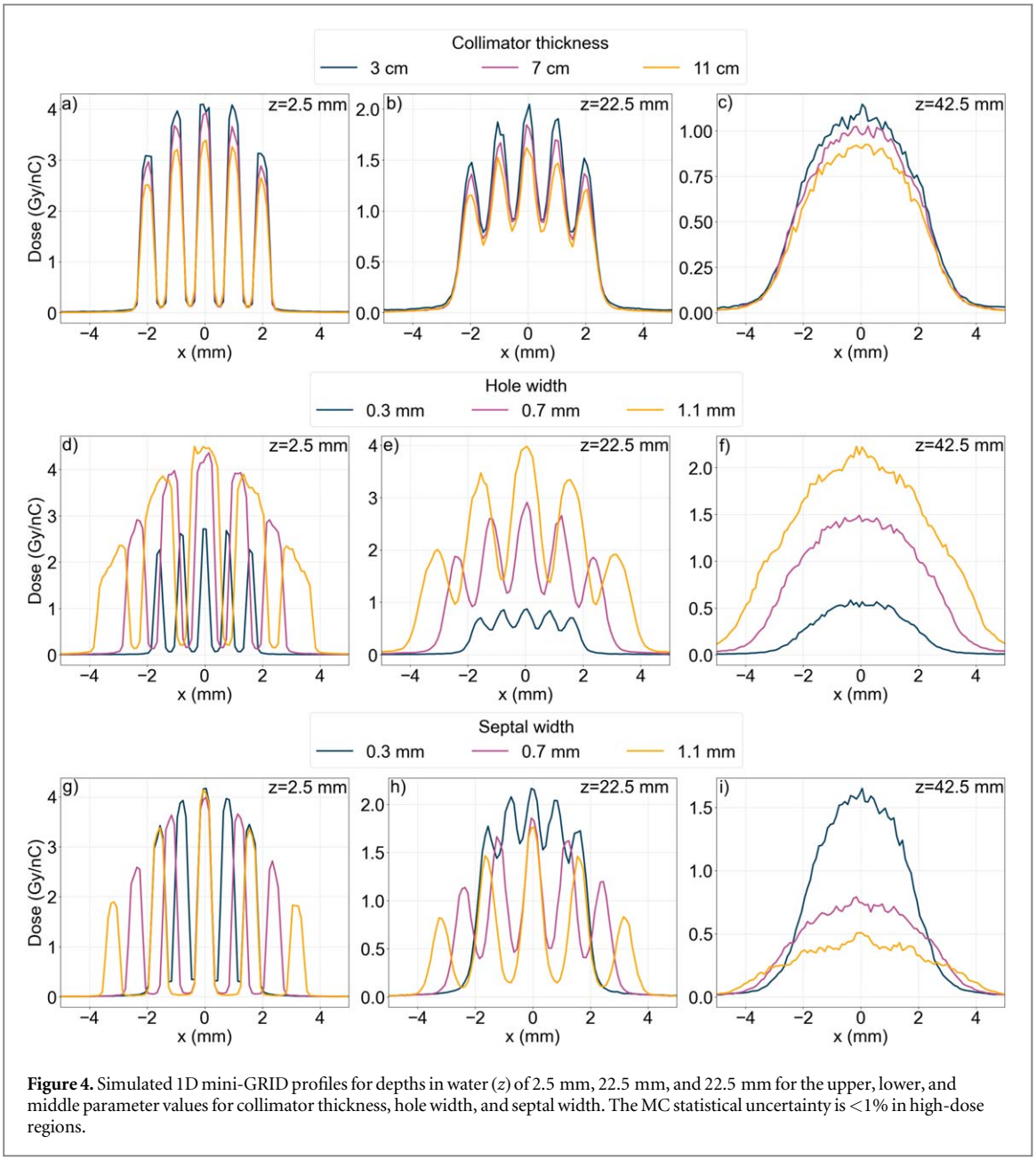

Figure 4. Simulated 1D mini-GRID profiles for depths in water (z) of 2.5 mm, 22.5 mm, and 22.5 mm for the upper, lower, and middle parameter values for collimator thickness, hole width, and septal width. The MC statistical uncertainty is <1% in high-dose regions.

beam case, the σ_x and σ_y values as a function of depth were also compared to films. For the mini-GRID case, valley dose and PVDR were also compared.

For these simulations, the physics list was expanded to include neutron physics and the cutoff distance was decreased due to smaller water phantom voxels. The physics list comprised the following modules 'g4em-standard_opt4', 'g4h-phy_QGSP_BIC_HP', 'g4decay', 'g4ion-binarycascade', 'g4h-elastic_HP', 'g4stopping', 'g4radioactivedecay', and 'g4em-extra' and the cutoff distance was set to 0.004 cm for all particles.

3. Results

3.1. Mini-GRID collimator optimization

1D-profiles across the center of the mini-GRID dose distributions are plotted for all of the optimization values tested for each parameter at water depths (z) of 2.5 mm, 22.5 mm, and 42.5 mm (see figure 4).

The collimator thickness plot at $z = 2.5$ mm depth in figure 4(a) revealed distinct peaks and valleys which perfectly overlapped in x, but peak and valley doses varied for the different collimator thicknesses. The $z = 22.5$ mm depth plot in figure 4(b) displayed much higher valley doses (nearing 1 Gy nC^{-1}) with peaks and valleys still presenting similar overlap in x for all thicknesses. At the $z = 42.5$ mm depth (figure 4(c)), the peaks

and valleys were essentially indistinguishable for all collimator thicknesses and a Gaussian-like profile remained which decreased in dose for longer collimators.

In the hole width study, the $z = 2.5$ mm plots (figure 4(d)) presented vastly different peak and valley doses, as well as peak widths for the tested hole widths. Due to the collimator design, the effective size of the mini-GRID field was larger for larger hole widths. At the $z = 22.5$ mm depth (figure 4(e)), the profiles display much higher valley doses and lower peak doses, in particular for the smaller holes. At $z = 42.5$ mm (figure 4(f)), peaks and valleys could not be distinguished and Gaussian-like profiles decreasing in output and widening in beam size were observed.

The $z = 2.5$ mm plots (figure 4(g)) in the septal width study presented distinct peaks and valleys with similar peak widths across the collimators. As expected, the effective field size was larger for larger septal widths. At $z = 22.5$ mm depth (figure 4(h)), the valley dose was higher for all collimators but it was particularly increased for the smaller septal widths. Similar to the collimator thickness and hole width parameter variations, the plots at $z = 42.5$ mm depth for septal widths (figure 4(i)) presented no discernible peaks and valleys for any septal width. The profiles were Gaussian-like with dose decreasing and width increasing with increasing septal width.

Mean peak dose per charge, mean valley dose per charge, and PVDR as functions of depth in the water phantom for all tested values of collimator thickness, hole width, and septal width are shown in figure 5. Figure 5(a) presented higher surface peak doses for larger collimator thicknesses. Each collimator followed a very similar trend with depth. The peak dose initially decayed until ∼30 mm depth where the peak dose decrease became less sharp. The peak dose per charge at 2.5 mm depth was 3.15 ± 0.04 Gy nC^{-1} for the 3 cm thick collimator and 2.55 ± 0.03 Gy nC^{-1} for the 11 cm thick collimator. In figure 5(b), the valley doses for all collimator thicknesses were statistically indistinguishable at shallow depths, followed by a sharp increase until a maximum was reached at ∼35 mm depth, noting that the maximum valley dose was 1.17× larger for the 3 cm collimator compared to the 11 cm collimator. Past $z \approx 35$ mm depth, the valley dose decreased with approximately the same slope for all collimators. In figure 5(c), the PVDR decreases similarly for all collimator thicknesses and it converges to an ultimate plateau of PVDR ≈ 1.

The peak dose fall-off as a function of depth for different collimator hole widths is presented in figure 5(d). The hole widths, in order from highest to lowest initial peak dose, were 0.5 mm, 0.7 mm, 0.9 mm, 1.1 mm, and 0.3 mm. However, smaller hole widths presented a steeper dose fall-off causing a cross-over of multiple curves ultimately resulting in larger hole widths having higher peak doses past depths of ≈30 mm. The valley dose plots in figure 5(e) presented low initial values for all hole widths which were followed by a steep increase until ultimately reaching a maximum and followed by a gradual decrease with steeper slopes for larger hole widths. Considering the extreme cases, the 1.1 mm hole width collimator had a maximum valley dose per charge of 1.35 ± 0.09 Gy nC^{-1}, whereas the 0.3 mm hole width collimator had a maximum valley dose per charge of 0.49 ± 0.01 Gy nC^{-1}. The PVDR plots (figure 5(f)) revealed that the 0.3 mm hole width presented a surface PVDR of 39.4 ± 1.4 and the 1.1 mm hole width case had a surface PVDR of 18.9 ± 1.3.

In the septal width study, the peak dose plots as functions of depth in figure 5(g) demonstrated that larger septal widths produced lower peak doses. Examining the extreme cases, the surface peak dose was 3.38 ± 0.03 Gy nC^{-1} for the 0.3 mm septal width collimator and 2.05 ± 0.06 Gy nC^{-1} for the 11 mm septal width collimator. In all cases, the peak dose rapidly decreased with depth, ultimately reaching a point at $z \approx 30$ mm past which the decrease in peak dose became less steep. The depths at which this point was reached increased with septal width and the slopes of the final part of the curves decreased with septal width. The valley dose curves in figure 5(h) showed that larger septal widths presented notable increases in the depth at which the valley dose began to sharply increase, as well as decreases of the maximum valley dose. The maximum valley dose was 0.26 ± 0.02 Gy nC^{-1} for the 1.1 mm septal width collimator and 1.42 ± 0.03 Gy nC^{-1} for the 0.3 mm septal width case. The PVDR plot in figure 5(i) showed that septal width had the biggest impact on PVDR.

For each tested parameter, depth of convergence (PVDR $\leqslant 1.1$) was also calculated to study how deep spatial fractionation is maintained, the results are presented in table 4. Surface PVDR for each collimator is also presented in table 4.

3.2. Film dosimetry at CLEAR

2D open beam and mini-GRID dose rate distributions from the films irradiated at 200, 175, and 140 MeV at CLEAR are presented in figure 6.

The 2D dose rate distributions for the open beam irradiations presented well-formed Gaussian beams for 200 MeV and 175 MeV with a slight misshaping for the 140 MeV beam. At 13 mm depth, the beam sizes were $\sigma_x = (4.12 \pm 0.20)$ mm and $\sigma_y = 4.01 \pm 0.20$ mm, $\sigma_x = (4.63 \pm 0.26)$ mm and $\sigma_y = (4.67 \pm 0.27)$ mm, and $\sigma_x = (5.70 \pm 0.26)$ and $\sigma_y = (5.50 \pm 0.27)$ mm for 200, 175, and 140 MeV, respectively. The 2D mini-GRID profiles for 200 MeV and 175 MeV presented well-centred dose rate distributions with some misshaping of the beam for 140 MeV where the highest dose rate was seen in the corner of the collimator. For all energies, the peaks

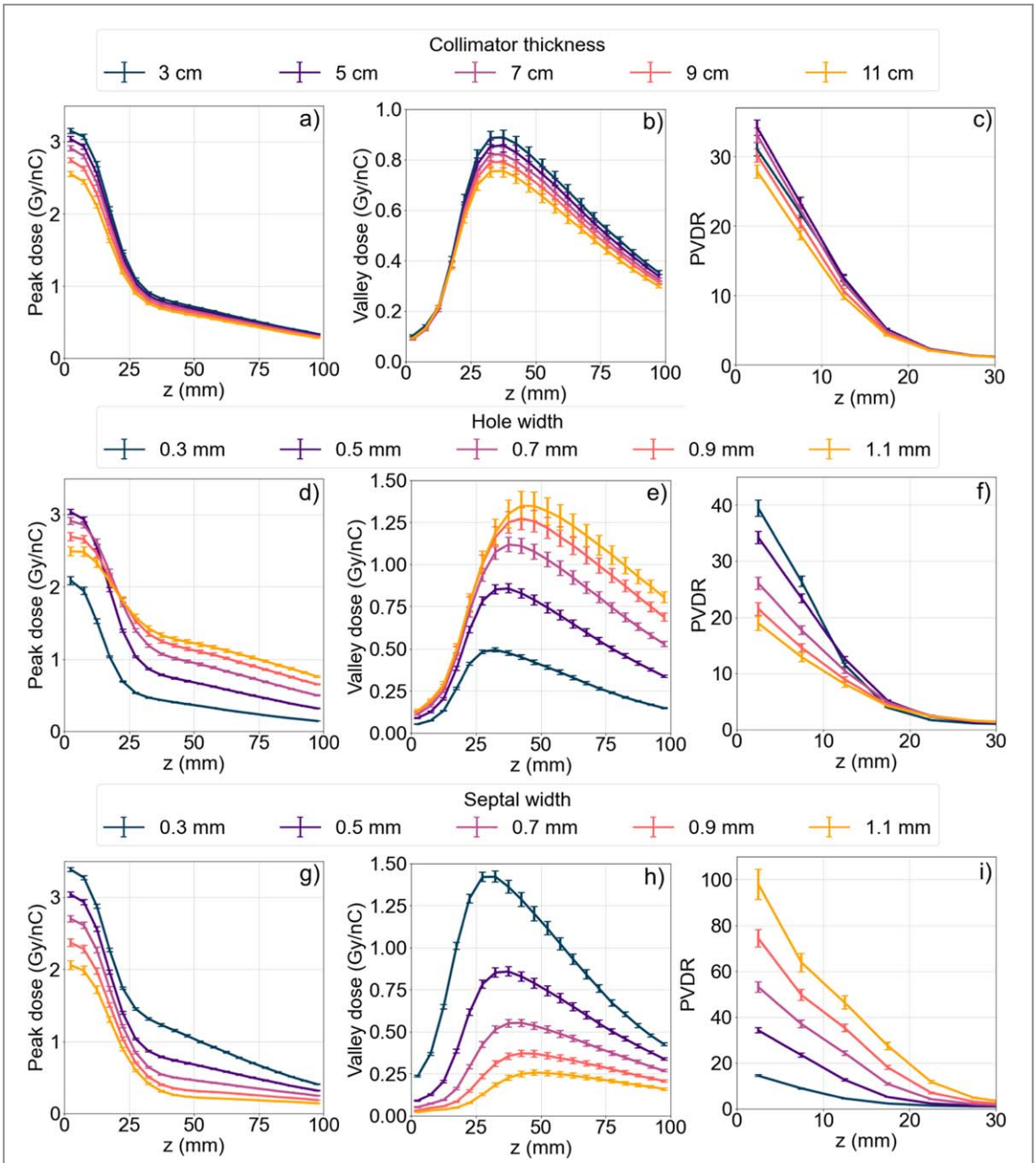

Figure 5. Simulated mean peak and valley dose per charge and PVDR as functions of depth in water for all tested parameter values for collimator thickness, hole width, and septal width. The MC statistical uncertainty is <1% on the calculated quantities.

Table 4. Surface PVDR ($z = 2.5$ mm) and depths of convergence (DoC) for the tested values of collimator thickness, hole width, and septal width.

Col. thickness	Surface PVDR	DoC	Hole width	Surface PVDR	DoC	Septal width	Surface PVDR	DoC
3 cm	31 ± 1	31.0 mm	0.3 mm	39 ± 1	27.5 mm	0.3 mm	14 ± 1	26.0 mm
5 cm	34 ± 1	30.8 mm	0.5 mm	34 ± 1	30.8 mm	0.5 mm	34 ± 1	30.8 mm
7 cm	33 ± 1	30.8 mm	0.7 mm	26 ± 1	32.6 mm	0.7 mm	53 ± 2	34.9 mm
9 cm	30 ± 1	30.6 mm	0.9 mm	22 ± 1	34.2 mm	0.9 mm	74 ± 4	38.0 mm
11 cm	28 ± 1	30.4 mm	1.1 mm	19 ± 1	35.1 mm	1.1 mm	98 ± 7	41.1 mm

were well-defined at 13 mm depth, distinguishable at 33 mm depth, and no peaks or valleys could be visually identified at $z = 63$ mm.

1D-profiles across the center of the Gaussian dose rate distributions in x at 13 mm, 33 mm, and 63 mm depths for 200, 175, and 140 MeV open beam and mini-GRID irradiations are shown in the top row of figure 7.

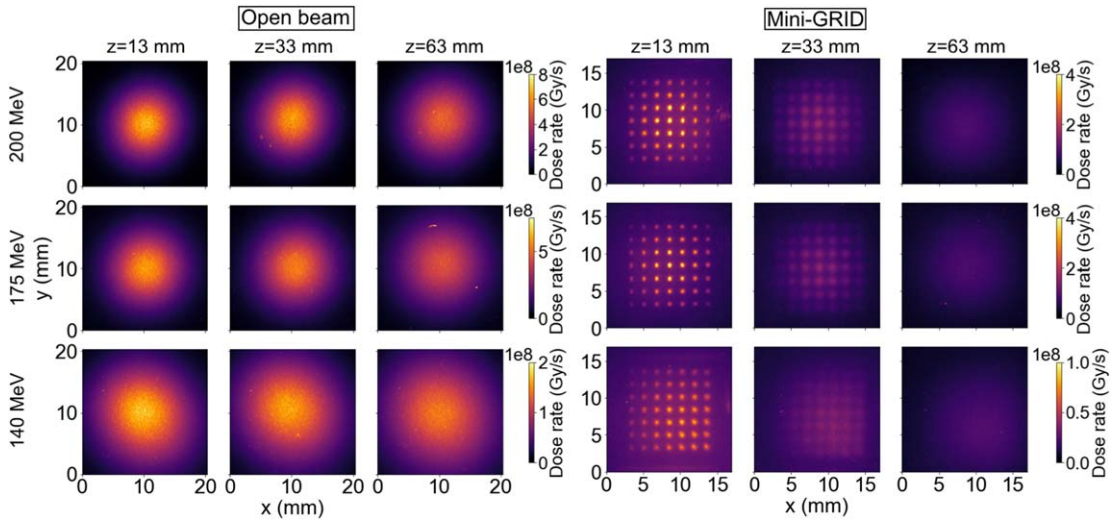

Figure 6. 2D open beam and mini-GRID dose rate profiles from radiochromic films at 13 mm, 33 mm, and 63 mm depths for 200 MeV, 175 MeV, and 140 MeV.

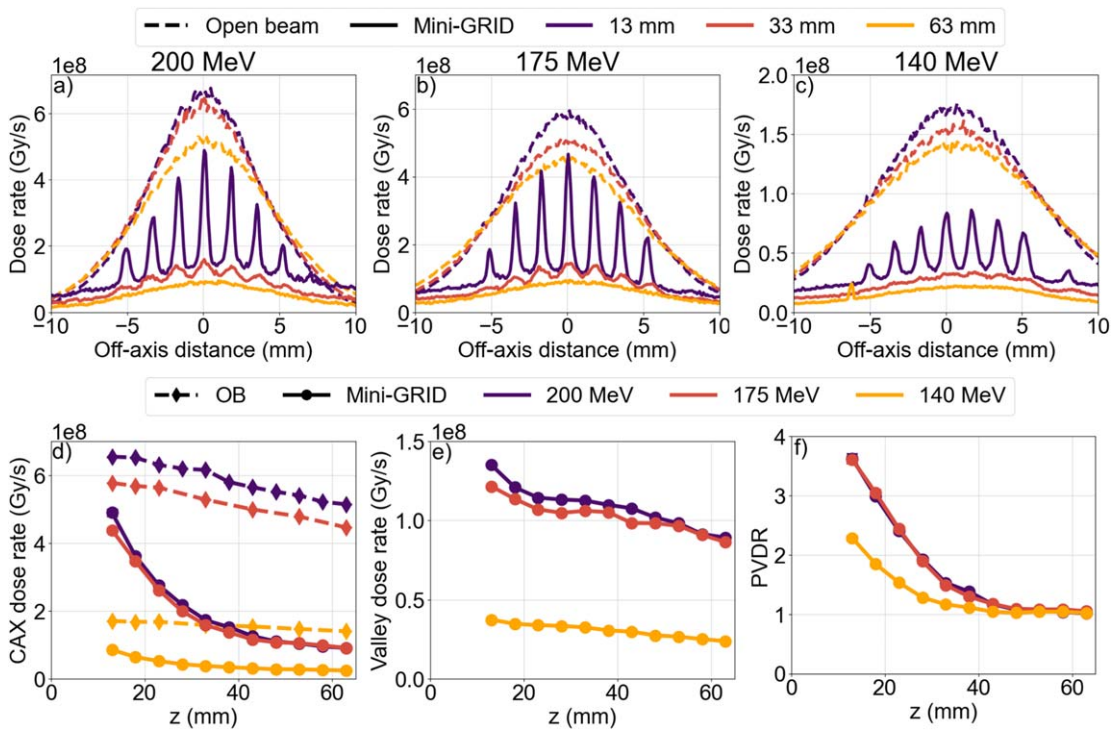

Figure 7. 1D mini-GRID and open beam dose rate profiles across the center of the beam from EBT3 GAFChromic films at 13 mm, 33 mm, and 63 mm depths for (a) 200 MeV, (b) 175 MeV, and (c) 140 MeV. (d) Central axis dose rate, (e) valley dose rate, and (f) PVDR as functions of depth in water.

The central axis dose rate, valley dose rate, and PVDR were plotted as functions of depth for 200 MeV, 175 MeV, and 140 MeV in the bottom row of figure 7.

The 200 MeV open beam profiles (figure 7(a)) presented the highest dose rates of the three energies at all depths. The dose rate drop-off with depth was evident in both mini-GRID and open beam profiles. For the mini-GRID irradiation, CAX dose rate decreased by a factor of ~2.2 from 13 to 33 mm depth, and at 63 mm depth, no peaks or valleys were seen. For the 175 MeV irradiation (figure 7(b)), similar trends were seen. In the open beam irradiations, the 175 MeV CAX dose rate fall-off was more pronounced between 13 mm to 33 mm depth than was seen at 200 MeV. The mini-GRID profiles were very similar to the 200 MeV case. In agreement with 200 MeV, the 63 mm mini-GRID plot presents no distinguishable peaks or valleys. The 140 MeV 1D profiles (figure 7(c)) show a larger beam size compared to the 200 MeV and 175 MeV open beam profiles. The peak and

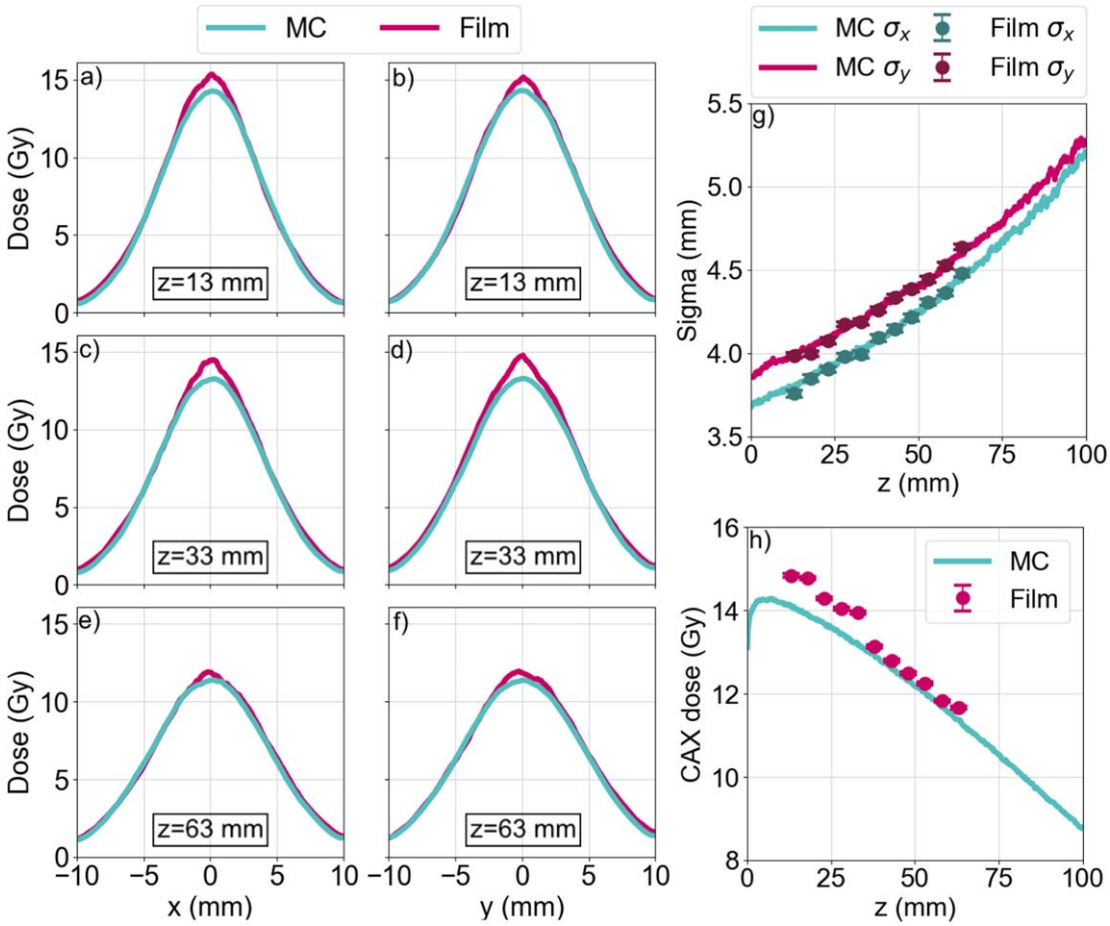

Figure 8. Open beam profiles from simulation and from film measurements at (a) and (b) 13 mm, (c) and (d) 33 mm, and (e) and (f) 63 mm depths. (g) σ_x and σ_y with depth in water from simulation and film measurements. (h) Central axis dose with depth for MC simulation and film measurements. The MC statistical uncertainty is <1% in high dose regions and for the calculated quantities.

valley dose rates at 13 mm depth are more similar for 140 MeV than for 200 MeV and 175 MeV. At 33 mm depth, the mini-GRID profile peaks are barely identifiable and finally at 63 mm depth no peaks or valleys are seen.

The open beam central axis dose rates shown in figure 7(d) presented relatively linear decreases for all energies with higher dose rates measured at the higher energies. The 200 MeV and 175 MeV mini-GRID CAX dose plots presented similar trends with the 200 MeV CAX dose rates being ~1.1× larger than 175 MeV. At 13 mm depth, the 200 MeV mini-GRID maximum dose rate was $(4.90 \pm 0.11) \times 10^8$ Gy s^{-1}, the 175 MeV mini-GRID maximum dose rate was $(4.38 \pm 0.08) \times 10^8$ Gy s^{-1} dose rate, and the 140 MeV mini-GRID maximum dose rate was $(0.85 \pm 0.02) \times 10^8$ Gy s^{-1}. For all energies, the mini-GRID CAX dose rates decreased exponentially until reaching a linear decrease similar to the open beam cases. Notably, the 140 MeV exponential fall-off was slower compared to 175 MeV and 200 MeV. The valley dose rates showed relatively similar trends across the three energies, with approximately linear decreases with depth. The valley dose rate was highest for 200 MeV, followed by 175 MeV and the 140 MeV valley dose rate was ~3× lower than for 200 and 175 MeV. At 13 mm depth, the valley dose rates were $(1.35 \pm 0.01) \times 10^8$ Gy s^{-1}, $(1.22 \pm 0.01) \times 10^8$ Gy s^{-1} and $(0.37 \pm 0.01) \times 10^8$ Gy s^{-1} for 200 MeV, 175 MeV, and 140 MeV, respectively. Finally, PVDR (figure 7(f)) decreased sharply with depth before plateauing at PVDR ≈1 for all energies. PVDRs at 13 mm depth were 3.63 ± 0.08, 3.61 ± 0.07, and 2.29 ± 0.05 for 200, 175, and 140 MeV, respectively. The approximate depths of convergence (PVDR ⩽ 1.1) were 47 mm, 47 mm, and 39 mm for 200 MeV, 175 MeV, and 140 MeV, respectively.

3.3. MC simulations of the 200 MeV CLEAR beam

Film and MC-simulated open beam 1D-profiles at 13 mm, 33 mm, and 63 mm depths in water phantom are shown in figures 8(a)–(f) and simulated and measured at water depths from 0 to 100 mm are shown in figure 8(g). Figure 8(h) shows simulated and measured CAX depth dose.

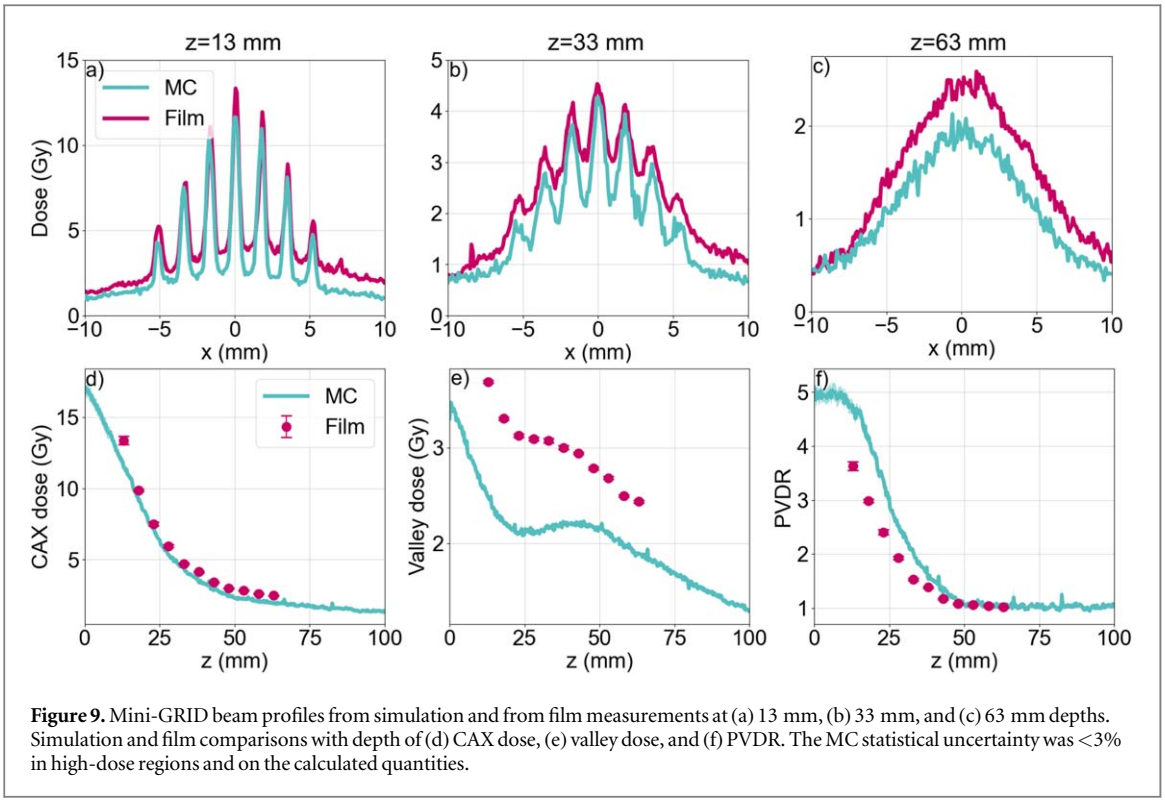

Figure 9. Mini-GRID beam profiles from simulation and from film measurements at (a) 13 mm, (b) 33 mm, and (c) 63 mm depths. Simulation and film comparisons with depth of (d) CAX dose, (e) valley dose, and (f) PVDR. The MC statistical uncertainty was <3% in high-dose regions and on the calculated quantities.

For both open beam and mini-GRID cases, the measurements presented higher doses. The mean difference in σ_x and σ_y between open beam simulations and films for all depths was 0.5% and the mean CAX dose difference was 3% higher for films.

Film and simulated mini-GRID 1D profiles at depths of 13 mm, 33 mm, and 63 mm are shown in figures 9(a)–(c). CAX depth dose is presented in figure 9(d), valley depth dose in figure 9(e), and PVDR as a function of depth is shown in figure 9(f).

For mini-GRID experiments, the mean film CAX dose was 14% higher, the valley dose was 27% higher and the PVDR was 14% lower than in simulations.

4. Discussion

This study considered UHDR mini-GRID radiotherapy using a VHEE source. Such a technique has the potential to widen the therapeutic window of radiation therapy, if capable of synergizing FLASH RT and SFRT. Firstly, a mini-GRID collimator was optimized and 3D-printed for mini-GRID film dosimetry with a UHDR VHEE source.

The optimized mini-GRID collimator, which was 3D-printed out of tungsten and used for film irradiations with the CLEAR beamline, was designed based on the achievable beam sizes at CLEAR (Korysko *et al* 2023) and the parameter variation results presented in section 3.1. The ideal mini-GRID collimator would maximize PVDR and minimize valley dose since these have all been shown to be driving factors in maximizing the tissue-sparing effects seen in SFRT (Dilmanian *et al* 2002, Fernandez-Palomo *et al* 2022). Ideally, PVDR would remain high throughout the patient; since this is not easily achieved, another metric that was considered was the depth of convergence (PVDR $\leqslant$ 1.1). The depths of convergence seen in the parameter variations were relatively low (for clinical tumour depths) so increasing this depth was a primary driver in our choices as well. In addition to these factors, the profile would also hopefully be flat across mini-GRID peaks to improve the uniformity in the tumour. Beam flatness could be improved by employing a flattening filter which is currently being developed for CLEAR (Robertson *et al* 2023).

The first parameter that was chosen for the optimized mini-GRID collimator was the septal width. A 1.1 mm septal width was chosen because it provided a reduction in valley dose (~5.5 $\times$ lower maximum valley dose as compared to 0.3 mm septal widths) without as much compromise in peak dose (~1.6$\times$ lower surface peak dose as compared to 0.3 mm septal width) as seen in figure 5. Larger septal widths greatly increased PVDR and also increased the depth of convergence (see table 4).

The next parameter that was chosen was the hole width of 0.5 mm. In the parameter variation (see figure 5), the mini-GRID collimator with the 0.5 mm hole width presented the highest peak dose, the second lowest valley

dose, the second highest initial PVDR, but also, unfortunately, the second shallowest depth of convergence. Since a 1.1 mm septal width with a large depth of convergence was already chosen, this compromise was deemed reasonable.

The thickness of the fabricated mini-GRID collimator was chosen to be 20 mm, a value outside of the range considered in the parameter variation. This small thickness was chosen because shorter collimators were seen to maximize peak dose, though unfortunately at the cost of having the highest valley dose with minimal PVDR improvement, albeit with the greatest depth of convergence (see figure 5 and table 4). The $z = 2.5$ mm peak dose for the 30 mm collimator was 1.23× higher than for the 110 mm collimator, whereas the maximum valley dose was 1.17× higher. Since the increase in peak dose was more significant, this shorter collimator choice was deemed reasonable. The slight increase in depth of convergence, which was seen as mini-GRID collimators were shortened, was an added benefit. In addition to these geometric parameters, the collimator was made a rectangular prism instead of a cylinder to facilitate alignment and holding. The holes also comprised a 7×7 array rather than 5×5, to increase the number of peaks and thus field size.

The film irradiations presented instantaneous peak and valley dose rates on the order of 10^8 Gy s^{-1}, well above the nominal mean ultra-high dose rate threshold of 40 Gy s^{-1} found in FLASH literature (Wilson *et al* 2020). In figure 7(d), the CAX dose rates for mini-GRID rapidly fell off and plateaued at around 40 mm depth in water, as compared to the open beam irradiations which featured slow linear decreases in CAX dose rate. The rapid fall-off in CAX dose rate for the mini-GRID irradiations as compared to the open beam irradiations is simply a result of field size. The roughly linear decrease in valley dose rates seems to follow a similar trend as for the open beam CAX dose rate profiles, suggesting that both begin obeying similar dose fall-offs.

The PVDRs at 13 mm depth for all energies were lower than expected based on the collimator optimization PVDRs. This is likely due to the lack of beam divergence in simulations that resulted in higher PVDRs. Beam divergence ultimately reduces peak dose and causes it to decrease more quickly with depth while also increasing valley doses and the rate at which it increases with depth. MC simulations of the irradiations with a more accurate beam definition presented more similar PVDRs to those seen in experiments.

The open beam simulation results presented in figure 8 showed excellent agreement in σ_x, σ_y with films with 0.5% difference on average, which was a result of the beam divergence and initial σ_x, σ_y being adjusted to achieve such an agreement. The CAX dose rate plot in figure 8(h) had a slightly worse agreement (3% difference on average) and the agreement for depths <30 mm was notably worse than for deeper depths. The 1D beam profiles suggest that the CLEAR beam measured on film was not a perfect Gaussian and presented a sharper peak which appeared to flatten with depth. This could be due to electron leakage through the beam shutter which was also observed in more recent CLEAR experiments. The open beam 1D profiles in figures 8(a)–(f) also showcase the agreement in σ_x, σ_y and the slightly worse agreement between the CAX doses. The mini-GRID simulation results presented in figure 9 showed higher film doses than in simulation, similar to the open beam results. In particular, the experimental valley dose was 27% higher on film than in simulation, as compared to the experimental peak (CAX) dose which was 14% higher. The experimental valley doses were significantly higher compared to the CAX doses. The higher CAX and valley film dose could be the result of the Bremsstrahlung photon dose (from collimator interactions) captured on film not being analyzed correctly since the film calibration was done for a 5.5 MeV linac electron beam. The valleys would, in that case, show worse agreement due to them having a higher percentage of the dose being from Bremsstrahlung photons. This conclusion is in agreement with a study by Sorriaux *etal.* who showed that for the same optical density, electrons deliver a higher dose than photons (Sorriaux *et al* 2013). Additional TOPAS simulations were performed to determine the percentage of Bremsstrahlung photon dose contributing to the total dose to confirm this hypothesis. The Bremsstrahlung photon valley dose from 13 mm to 63 mm contributed to the total dose by 51%. Between these depths, it decreased exponentially from 79% to 35% and the discrepancy between films and simulations decreased from 32% to 22%. The valley dose discrepancy as a function of Bremsstrahlung photon dose appeared to show a reasonable correlation between Bremsstrahlung photon dose and the discrepancy between simulation and film, supporting our hypothesis. For the CAX dose, on average 27% of the dose was due to Bremsstrahlung photons between $z = 13$ mm and $z = 63$ mm, much lower than for valleys where 51% of the dose was due to Bremsstrahlung photons. This supported our hypothesis that the discrepancy between film and simulations was due to Bremsstrahlung photons since valleys showcased a larger discrepancy than the CAX dose did.

The depths of convergence (47 mm for 200 MeV) and PVDRs (figure 7(f)) that were achieved in this study are likely too low for GRID-fractionation to reach deep-seated tumours. A considerable benefit of potential VHEE treatments is the slower depth-dose fall-off compared to clinical photon beams (Whitmore *et al* 2021) allowing for effective treatment of deep-seated tumours. The depth of convergence and PVDR would require improvement for GRID VHEE normal tissue sparing. Additionally, the small field sizes that existing VHEE sources are currently limited to reduce the number of patient cases in which open beam VHEE treatments could be applicable. Nevertheless, small tumours may be an apt fit for these treatment modalities until new accelerator technology allows for increased field sizes. Given the potential for FLASH and SFRT tissue-sparing effects, these

treatments could still be well-suited to tumours near critical structures, but at shallow patient depths. Further collimator optimization, focused on maintaining spatial fractionation with depth could prove of value for improving the potential for such a technique. Another avenue to SFRT using VHEEs is pencil beam scanning, which could improve PVDR by reducing the valley dose due to the Bremsstrahlung photons produced in the collimator while also increasing the effective GRID field size.

5. Conclusion

In this study, Monte Carlo simulations were used to optimize the geometric parameters of a mini-GRID collimator for irradiations with very-high-energy electrons at ultra-high dose rates. The optimized 3D-printed tungsten mini-GRID collimator was used for VHEE film irradiations at the CLEAR user facility at CERN. Open beam and mini-GRID irradiations were performed at 200, 175, and 140 MeV and later replicated in MC simulation. Instantaneous dose rates on the order of 100 MGy s^{-1} were achieved, encouraging future UHDR irradiations, however, the PVDRs and depths of convergences achieved in this study were determined to likely be too low for a significant potential for SFRT tissue-sparing effects, particularly at depth. Given the current limitations in field size for VHEE source, VHEE mini-GRID treatments would therefore only possibly be suitable for small tumours at depths shallower than the depth of convergence to maintain spatial fractionation in normal tissues. To improve the PVDRs and potential for SFRT tissue-sparing effects, further optimization or new means of achieving spatial fractionation are required. For example, pencil beam scanning to achieve a higher degree of spatial fractionation with reduced valley doses while still delivering at UHDRs could be a feasible solution for VHEE SFRT in the future.

Acknowledgments

This work was funded in part by an NSERC Discovery Grant as well as the Canada Research Chairs program. This research was enabled in part by support provided by WestGrid (www.westgrid.ca) and The Digital Research Alliance of Canada (formerly known as Compute Canada) (www.alliancecan.ca).

Data availability statement

The data cannot be made publicly available upon publication because they are not available in a format that is sufficiently accessible or reusable by other researchers. The data that support the findings of this study are available upon reasonable request from the authors.

ORCID iDs

Nathan Clements https://orcid.org/0000-0001-8911-997X
Nolan Esplen https://orcid.org/0000-0002-8347-8653
Joseph Bateman https://orcid.org/0000-0002-5967-6748
Manjit Dosanjh https://orcid.org/0000-0003-1378-349X
Pierre Korysko https://orcid.org/0000-0002-7878-2298
Roberto Corsini https://orcid.org/0000-0002-0934-8199
Magdalena Bazalova-Carter https://orcid.org/0000-0002-9365-2889

References

Adrian G, Konradsson E, Lempart M, Bäck S, Ceberg C and Petersson K 2020 The FLASH effect depends on oxygen concentration *Br. J. Radiol.* **93** 20190702

Bazalova-Carter M and Esplen N 2019 On the capabilities of conventional x-ray tubes to deliver ultra-high (FLASH) dose rates *Med. Phys.* **46** 5690–5

Bazalova-Carter M, Qu B, Palma B, HÅrdemark B, Hynning E, Jensen C, Maxim P G and Loo B W 2015 Treatment planning for radiotherapy with very high-energy electron beams and comparison of VHEE and VMAT plans *Med. Phys.* **42** 2615–25

Bazalova-Carter M *et al* 2015 Comparison of film measurements and Monte Carlo simulations of dose delivered with very high-energy electron beams in a polystyrene phantom *Med. Phys.* **42** 1606–13

Berger M, Coursey J and Zucker M 1999 Stopping-power & range tables for electrons, protons, and helium ions *NIST Standard Reference Database 124* (http://physics.nist.gov/Star)

Beyreuther E, Brand M, Hans S, Hideghéty K, Karsch L, Leßmann E, Schürer M, Szabó E R and Pawelke J 2019 Feasibility of proton FLASH effect tested by zebrafish embryo irradiation *Radiother. Oncol.* **139** 46–50

Billena C and Khan A J 2019 A current review of spatial fractionation: back to the future? *Int. J. Radiat. Oncol. Biol. Phys.* **104** 177–87

Böhlen T T, Germond J F, Bourhis J, Vozenin M C, Ozsahin E M, Bochud F, Bailat C and Moeckli R 2022 Normal tissue sparing by FLASH as a function of single-fraction dose: a quantitative analysis *Int. J. Radiat. Oncol. Biol. Phys.* **114** 1032–44

Boscolo D, Scifoni E, Durante M, Krämer M and Fuss M C 2021 May oxygen depletion explain the FLASH effect? a chemical track structure analysis *Radiother. Oncol.* **162** 68–75

Bronk J *et al* 2022 Enhanced radiation-sparing effects of ultra-high dose rate proton radiation (FLASH-RT) in a human induced pluripotent stem cell-derived cerebral organoid model *Int. J. Radiat. Oncol. Biol. Phys.* **114** S66

Buonanno M, Grilj V and Brenner D J 2019 Biological effects in normal cells exposed to FLASH dose rate protons *Radiother. Oncol.* **139** 51–5

Casolaro P, Campajola L, Breglio G, Buontempo S, Consales M, Cusano A, Cutolo A, Di Capua F, Fienga F and Vaiano P 2019 Real-time dosimetry with radiochromic films *Sci. Rep.* **9** 1–11

Choi J I, Daniels J, Cohen D, Li Y, Ha C S and Eng T Y 2019 Clinical outcomes of spatially fractionated GRID radiotherapy in the treatment of bulky tumors of the head and neck *Cureus* **11** e4637

Clements N, Bazalova-Carter M and Esplen N 2022 Monte Carlo optimization of a GRID collimator for preclinical megavoltage ultra-high dose rate spatially-fractionated radiation therapy *Phys. Med. Biol.* **67** 185001

Clements N, Esplen N and Bazalova-Carter M 2023 A feasibility study of ultra-high dose rate mini-GRID therapy using very-high-energy electron beams for a simulated pediatric brain case *Phys. Med.* **112** 102637

Corsini R, Farabolini W, Gilardi A, Dyks L A, Korysko P and Switzerland K N S 2021 Status of vhee radiotherapy related studies at the clear user facility at CERN *Proc. of IPAC2021, Campinas* pp 2704–7

DesRosiers C, Moskvin V, Bielajew A F and Papiez L 2000 150–250 MeV electron beams in radiation therapy *Phys. Med. Biol.* **45** 1781

DesRosiers C, Moskvin V, Cao M, Joshi C J and Langer M 2008 Laser-plasma generated very high energy electrons in radiation therapy of the prostate *Proc. SPIE Commercial and Biomedical Applications of Ultrafast Lasers VIII* **6881** 688109

Dilmanian F A, Morris G M, Zhong N, Bacarian T, Hainfeld J F, Kalef-Ezra J, Brewington L J, Tammam J and Rosen E M 2003 Murine EMT-6 carcinoma: high therapeutic efficacy of microbeam radiation therapy *Radiation Research* **159** 632–41

Dilmanian F A *et al* 2002 Response of rat intracranial 9L gliosarcoma to microbeam radiation therapy *Neuro-Oncol.* **4** 26–38

Dunning C A and Bazalova-Carter M 2019 X-ray fluorescence computed tomography induced by photon, electron, and proton beams *IEEE Trans. Med. Imaging* **38** 2735–43

Esplen N, Mendonca M S and Bazalova-Carter M 2020 Physics and biology of ultrahigh dose-rate (FLASH) radiotherapy: a topical review *Phys. Med. Biol.* **65** 23TR03

Esplen N M, Egoriti L, Paley W, Planche T, Hoehr C, Gottberg A and Bazalova-Carter M 2022 Design optimization of an electron-to-photon conversion target for ultra-high dose rate x-ray (FLASH) experiments at TRIUMF *Phys. Med. Biol.* **67** 105003

Faddegon B, Ramos-Méndez J, Schuemann J, McNamara A, Shin J, Perl J and Paganetti H 2020 The TOPAS tool for particle simulation, a Monte Carlo simulation tool for physics, biology and clinical research *Phys. Med.: Eur. J. Med. Phys.* **72** 114–21

Favaudon V *et al* 2014 Ultrahigh dose-rate FLASH irradiation increases the differential response between normal and tumor tissue in mice *Sci. Transl. Med.* **6** 245ra93

Fernandez-Palomo C, Chang S and Prezado Y 2022 Should Peak Dose Be Used to Prescribe Spatially Fractionated Radiation Therapy?-A Review of Preclinical Studies *Cancers* **14** 3625

Hart A *et al* 2024 Plastic scintillator dosimetry of ultrahigh dose-rate 200 MeV electrons at CLEAR *IEEE Sensors* (https://doi.org/10.1109/JSEN.2024.3353190)

Korysko P *et al* 2023 The clear user facility: a review of the experimental methods and future plans *Proc. 14th Int. Particle Accelerator Conf., number 14 in IPAC'23-XIV Int. Particle Accelerator Conf. JACoW Publishing, Geneva, Switzerland* pp 876–9

Labarbe R, Hotoiu L, Barbier J and Favaudon V 2020 A physicochemical model of reaction kinetics supports peroxyl radical recombination as the main determinant of the FLASH effect *Radiother. Oncol.* **153** 303–10

Levy K, Rafat M, Casey K and Rankin E 2019 Total abdominal ultra-rapid flash irradiation decreases gastrointestinal toxicity compared to conventional radiation *Gynecologic Oncol.* **154** 75

Martínez-Rovira I, Fois G and Prezado Y 2015 Dosimetric evaluation of new approaches in GRID therapy using nonconventional radiation sources *Med. Phys.* **42** 685–93

Mohiuddin M, Fujita M, Regine W F, Megooni A S, Ibbott G S and Ahmed M M 1999 High-dose spatially-fractionated radiation (GRID): a new paradigm in the management of advanced cancers *Int. J. Radiat. Oncol. Biol. Phys.* **45** 721–7

Montay-Gruel P, Corde S, Laissue J A and Bazalova-Carter M 2022 FLASH radiotherapy with photon beams *Med. Phys.* **49** 2055–67

Neuner G, Mohiuddin M M, Vander Walde N, Goloubeva O, Ha J, Yu C X and Regine W F 2012 High-dose spatially fractionated GRID radiation therapy (SFGRT): a comparison of treatment outcomes with Cerrobend vs. MLC SFGRT *Int. J. Radiat. Oncol. Biol. Phys.* **82** 1642–9

Owen D *et al* 2022 Spatially fractionated radiation therapy in the modern era: the mayo clinic experience *Int. J. Radiat. Oncol. Biol. Phys.* **114** S86

Palma B, Bazalova-Carter M, Hardemark B, Hynning E, Qu B, Loo B W and Maxim P G 2016 Assessment of the quality of very high-energy electron radiotherapy planning *Radiother. Oncol. : J. Eur. Soc. Ther. Radiol. Oncol.* **119** 154–8

Papiez L, DesRosiers C and Moskvin V 2002 Very high energy electrons (50–250 MeV) and radiation therapy *Technology in Cancer Research & Treatment* **1** 105–10

Perl J, Shin J, Schümann J, Faddegon B and Paganetti H 2012 TOPAS: an innovative proton Monte Carlo platform for research and clinical applications *Med. Phys.* **39** 6818–37

Poppinga D, Kranzer R, Farabolini W, Gilardi A, Corsini R, Wyrwoll V, Looe H K, Delfs B, Gabrisch L and Poppe B 2020 VHEE beam dosimetry at CERN linear electron accelerator for research under ultra-high dose rate conditions *Biomed. Phys. Eng. Express* **7** 015012

Rahman M, Trigilio A, Franciosini G, Moeckli R, Zhang R and Böhlen T T 2022 FLASH radiotherapy treatment planning and models for electron beams *Radiother. Oncol.* **175** 210–21

Robertson C S, Burrows P N, Dosanjh M, Latina A and Gerbershagen A 2023 Beam optics study for a potential VHEE beam delivery system *J. Phys. Conf. Ser.* **2420** 012102

Ruan J L *et al* 2021 Irradiation at ultra-high (FLASH) dose rates reduces acute normal tissue toxicity in the mouse gastrointestinal system *Int. J. Radiat. Oncol. Biol. Phys.* **111** 1250–61

Schneider T, Fernandez-Palomo C, Bertho A, Fazzari J, Iturri L, Martin O A, Trappetti V, Djonov V and Prezado Y 2022 Combining FLASH and spatially fractionated radiation therapy: The best of both worlds *Radiother. Oncol. : J. Eur. Soc. Ther. Radiol. Oncol.* **175** 169–77

Schüler E, Acharya M, Montay-Gruel P, Loo B W, Vozenin M C and Maxim P G 2022 Ultra-high dose rate electron beams and the FLASH effect: from preclinical evidence to a new radiotherapy paradigm *Med. Phys.* **49** 2082–95

Schüler E, Eriksson K, Hynning E, Hancock S L, Hiniker S M, Bazalova-Carter M, Wong T, Le Q, Loo B W and Maxim P G 2017 Very high-energy electron (VHEE) beams in radiation therapy; Treatment plan comparison between VHEE, VMAT, and PPBS *Med. Phys.* **44** 2544–55

Smyth L M, Donoghue J F, Ventura J A, Livingstone J, Bailey T, Day L R, Crosbie J C and Rogers P A 2018 Comparative toxicity of synchrotron and conventional radiation therapy based on total and partial body irradiation in a murine model *Scientific Reports* **8** 12044

Smyth L M, Senthi S, Crosbie J C and Rogers P A 2016 The normal tissue effects of microbeam radiotherapy: what do we know, and what do we need to know to plan a human clinical trial? **92** 302–11

Sorriaux J, Kacperek A, Rossomme S, Lee J A, Bertrand D, Vynckier S and Sterpin E 2013 Evaluation of Gafchromic® EBT3 films characteristics in therapy photon, electron and proton beams *Phys. Med.* **29** 599–606

Tessonnier T *et al* 2021 FLASH dose rate helium ion beams: first *in vitro* investigations *Int. J. Radiat. Oncol. Biol. Phys.* **111** 1011–22

Vozenin M C, Hendry J H and Limoli C L 2019 Biological benefits of ultra-high dose rate flash radiotherapy: sleeping beauty awoken *Clin. Oncol.* **31** 407–15

Vozenin M C, Montay-Gruel P, Limoli C and Germond J F 2020 All irradiations that are ultra-high dose rate may not be FLASH: the critical importance of beam parameter characterization and in vivo validation of the FLASH effect *Radiat. Res.* **194** 571–2

Vozenin M C *et al* 2019 The advantage of FLASH radiotherapy confirmed in mini-pig and cat-cancer patients *Cancer Res.* **25** 35–42

Whitmore L, Mackay R I, van Herk M, Jones J K and Jones R M 2021 Focused VHEE (very high energy electron) beams and dose delivery for radiotherapy applications *Sci. Rep.* **11** 1–14

Widel M 2016 Radiation induced bystander effect: from in vitro studies to clinical application *Int. J. Med. Phys. Clin. Eng. Radiat. Oncol.* **5** 1–17

Wilson J D, Hammond E M, Higgins G S and Petersson K 2020 Ultra-High dose rate (FLASH) radiotherapy: silver bullet or fool's gold? *Front. Oncol.* **9** 1563

Wright M D, Romanelli P, Bravin A, Duc G L, Brauer-Krisch E, Requardt H, Bartzsch S, Hlushchuk R, Laissue J A and Djonov V 2021 Non-conventional ultra-high dose rate (FLASH) microbeam radiotherapy provides superior normal tissue sparing in rat lung compared to non-conventional ultra-high dose rate (FLASH) radiotherapy *Cureus* **13** e19317

Yan W *et al* 2020 Spatially fractionated radiation therapy: history, present and the future *Clin. Transl. Radiat. Oncol.* **20** 30–8

Yeboah C and Sandison G A 2002 Optimized treatment planning for prostate cancer comparing IMPT, VHEET and 15 MV IMXT *Phys. Med. Biol.* **47** 2247

Yeboah C, Sandison G A and Moskvin V 2002 Optimization of intensity-modulated very high energy (50–250 MeV) electron therapy *Phys. Med. Biol.* **47** 1285

Zhou S, Zheng D, Fan Q, Yan Y, Wang S, Lei Y, Besemer A, Zhou C and Enke C 2020 Minimum dose rate estimation for pulsed FLASH radiotherapy: a dimensional analysis *Med. Phys.* **47** 3243–9

GAFChromic EBT3 Film Specifications. Available at www.gafchromic.com 11/02/24